Mobile-aided screening system for proliferative diabetic retinopathy

Rahma Boukadida, Yaroub Elloumi, Mohamed Akil, Mohamed Hedi Bedoui

MAS-PDR: Mobile-Aided Screening System for Proliferative Diabetic Retinopathy

Rahma Boukadida[1]· Yaroub Elloumi[1,2,3] · Mohamed Akil[2] · Mohamed Hedi Bedoui[1]

Abstract

NeoVascularization (NV) occurs in the Proliferative Diabetic Retinopathy (PDR) stage, where the development progress of new vessels presents a high risk for severe vision loss and blindness. Therefore, early NV detection is primordial to preserve patient's vision. Several automated methods have been proposed to detect the NV on retinograph-captured fundus images. However, their employment is constrained by the reduced ophthalmologist per person ratio and the expensive equipment required for image capturing.

This paper presents a novel method for NV detection in smartphone-captured fundus images. The implementation of the method on a smartphone device having an optical lens for fundus capturing leads to a Mobiles -Aided-Screening system of PDR (MAS-PDR). The challenge is to ensure accurate and robust detection even with the moderate quality of fundus image, with a reduced execution time. Within this objective, we identify the major criteria of neovascularized vessels which are tortuosity, width, bifurcation and density. Our main contribution consists in proposing a sharp feature to reflect each criterion on reduced computational complexity processing. Therefore, the feature set is provided to a random forest classifier in order to deduce whether the fundus image is in the PDR stage.

A dataset raised from publicly databases is used on a 10-cross validation process where average accuracy of 98.69%, sensitivity of 97.73% and a specificity of 99.12% are achieved. To evaluate the method robustness, the same experimentation is repeated after applying motion blur filters to the fundus image dataset, where 98.91% accuracy, 96.75% sensitivity, and 100% specificity are deduced. Moreover, NV screening is performed under three seconds when executed in smartphone devices demonstrating the appropriateness of our suggested method to MAS-PDR.

Keywords: Fundus images · Neovascularization · Smartphone captured fundus image · Mobile-Aided-Screening (MAS) system ·Mobile Health · Random Forest (RF)

1. Introduction

Diabetes is a worldwide disease with more than 415 million of patients, according to a report of the international diabetes federation [1]. This number is expected to increase over the next decades to reach 642 million diabetics in 2040 [1, 2]. Diabetic Retinopathy (DR) is a serious complication of diabetes which affects nearly 30% of diabetes patients [3]. Moreover, the WHO has estimated that DR is the main responsible for 37 million cases of blindness throughout the world [4]. The DR can be divided into Non Proliferative Diabetic Retinopathy (NPDR) and Proliferative Diabetic Retinopahy (PDR). The latter is the most severe stage of DR, which corresponds to 9% of DR-affected people [3]. This stage is characterized by the proliferation of new abnormal blood vessels due to the extensive lack of oxygen in the retinal capillaries [5]. The Neovascularization (NV) can rapidly progress early PDR to advanced PDR that cause bleeding, fibrous proliferation, vitreous hemorrhage and retinal detachment, hence posing a high risk for severe vision loss and blindness [4, 6] . The detection of NV in early stage in order to stop or delay its progression leads to avoid vision loss and blindness.

NV diagnosis is based on examining fundus images, such as the ones shown in Fig.1. However, a delay in the diagnosis of patients on the PDR stage is registered. The first cause corresponds to the limited ratio of human and material resources per person required for fundus image acquisition and diagnosis. Besides, patients with PDR must mobilize to be diagnosed, which might be restricted due to the elderly DR patients and the geographical remoteness. In the literature, a lot of work has been proposed to detect NV [5, 7–15]. However, they are dedicated to classical fundus images, requiring ophthalmologists, capture equipment and patient mobility at the same time. Consequently, the proposed methods for NV diagnosis cannot retrieve the delay of NV diagnosis.

✉Yaroub Elloumi
yaroub.elloumi@esiee.fr
[1] Medical Technology and Image Processing Laboratory, Faculty of medicine, University of Monastir, Tunisia
[2] LIGM, Univ Gustave Eiffel, CNRS, ESIEE Paris, F-77454 Marne-la-Vallée, France
[3] ISITComHammam-Sousse, University of Sousse, Tunisia

This work was supported by the PHC-UTIQUE 19G1408 Research program.

The overuse of smartphones [16] and their growing performance in terms of processing, portability, storage capacity and image quality lead to be used in medicine, especially for ophthalmic screening. Various mobile digital retinal screening devices, such as iExaminer, D-EYE and Paxos digital ophthalmoscopes, have been suggested [17–19]. Those low-cost devices are composed by optical lens and designed to be attached to a smartphone. The smartphone captured fundus images are legible between 86% and 100% on average and have an accepted quality between 93% and 100% [20]. In addition, several clinical studies have approved the ability to detect DR from smartphone-captured fundus images [21–23]. However, those images are characterized by a moderate quality, caused by the handheld aspect of the capture process. Within this context, several methods have been put forward and implemented into smartphones to detect ocular pathologies, such as DR grading [22, 24] and glaucoma screening [25, 26].

Our objective consists in proposing a novel method that detects NV from smartphone-captured fundus images. The implementation of the method as an app on a smartphone associated with a mobile retinal screening device leads to propose Mobile-Aided-Screening (MAS) of PDR. The first challenge is to ensure an accurate detection even with the downgraded quality of smartphone-captured fundus images. The second challenge is to perform screening in a reduced time with respect to the clinical employment, despite the limited capacity of smartphone architectures.

The paper is organized in the following way. Section 2 discusses the related work. The suggested method for NV detection is presented in section 3. The evaluation of the proposed method using different fundus image databases and performance parameters is done in section 4, followed by conclusion in the last section.

2. Automated Methods for PDR Detection

2.1. Related work

Several automated methods for NV detection have been put forward in the literature. Some methods have aimed at NV screening while others have targeted the segmentation of neovascularized vessels, as detailed respectively in the following sub-sections. On the other hand, NV occurs on the Optic Disc (OD) before propagating into the whole retina. Accordingly, we observe that a lot of related work, whether for NV screening or vessel segmenting, has detected NV in the OD region, named "NV in optic Disc (NVD)". Others have focused on the neovascularized vessels in the whole retina, called "NV Elsewhere (NVE)". These methods are described respectively in each sub-section.

2.1.1. NV screening methods

The method proposed by Agurto et al. [7] selected the OD, enhanced the sub-image quality and segmented its vessels. After that, the features were extracted by applying the Amplitude-Modulation Frequency-Modulation (AM-FM) and granulometry, which were used to respectively analyze the vessel tortuosity and width. Finally, the partial least squares classifier was performed to deduce NV. In [12], a set of 1248 features were extracted from the OD through the AM-FM , fractal analysis and granulometry to model the vessel tortuosity, density and width. Then, the Support Vector Machine (SVM) classifier was performed to classify whether the fundus image was on the NVD stage.

For NVE screening methods, a study detailed in [9] presented a pixel wise classification method. A set of features was extracted for each pixel of the preprocessed image, which reflected the tortuosity and the retina texture through the standard deviation filters, the anisotropic

(a) **(b)**

Fig.1 Fundus images: **(a)** Healthy image, **(b)** PDR image

Gaussian filters, the Gabor matched filters and the differential invariant filters with multiple scales. Thereafter, the feature set was provided to the extreme learning machine to classify the fundus image as normal or neovascularized. To enhance the computational performance, the proposed method was implemented in parallel where two map-reduce models are employed respectively for feature extraction and training [27]. The work described in Yu et al. [15] consisted in extracting of 42 features: 34 reflecting the vessel shapes, five modeling the fractal dimension analysis and three representing granulometry analysis. After that, the recursive feature elimination algorithm is applied to select the set of the 18 optimal features. Thereafter, the SVM was used to classify whether the retinal image was neovascularized or not. Gupta et al. [14] proposed a method to identify NVE regions in the retinal image. A set of 525 features was extracted from each patch based on vessel density, width and tortuosity and on the retina texture. Thereafter, a Random Forest (RF) classifier was utilized to train the labeled patches. The method suggested in Hassan et al. [5] segmented the whole retinal vessel tree. Afterwards, the number and area of vessels were quantified. The fundus image was then split into regions where each was tested through the area and number values to deduce whether it contained neovascularized vessels.

2.1.2. Segmentation methods of neovascularized vessels

The method described in [13] focused on segmenting the abnormal vessels that belonged to the OD. In this context, several features were extracted from each segmented vessel to model the length, the width, the tortuosity and the density on it specific area. Other features were extracted from the whole vessel tree, which corresponded to the vessel number and the retina texture. Then, the SVM classifier intercepted the feature set to categorize a vessel as normal or neovascularized. The work described by Silkar et al. [11] propounded a method for the segmentation of neovascularized vessels inside the OD and elsewhere in the retina. In the first stage, the entire vessel map was split into two trees containing respectively the thick and thin vessels. After that, a threshold based on tortuosity and density was performed to the thin vessel tree in order to distinguish between normal and neovascularized ones.

The work described by Akram et al.[10] proceeded to segment the retinal vessel tree and extract features from each vessel to model their density, the number of vessels, the vessel tortuosity, the vessel width and the retina texture. Then, a multi-level m-Mediods classifier was used to differentiate normal and abnormal blood vessels. In [8], the fundus image was segmented using two approaches. From both vessel tree results, each vessel was distinguished in order to extract four features that were related respectively to the density, tortuosity and number of vessels and to the area. Those features were used to classify vessels into healthy or NV ones using the SVM. Finally, a vessel was considered as NV if it was classified as NV in both segmented vessel trees.

2.2. Critical study

The blood vessels converge from the optic nerve head into the whole retina. Hence, the abnormal vessels start to appear on the OD, which correspond to the early stage of PDR. Therefore, to screen the PDR, it is meaningful to detect NV on the OD rather than the whole retina.

The methods always segment the retina vessel. For the methods that target the neovascularized vessel segmentation, each vessel is extracted separately from the vessel tree in order to be classified. However, the methods aiming for NV screening proceed to extract summary features from the whole vessel tree [8, 9, 15] or from each tree region [5, 7, 11]. Those features may distort the detection by considering microvascular structures or vascular lesions, such as the ones occurring in the mild DR or in the wet aged macular degeneration stages, as abnormal vessels.

The NV detection approach are differentiated between methods in terms of considered vessel properties. Therefore, we study the existing methods in order to identify the NV properties, as indicated in Table 1. We deduce that some properties are more used than others, which are tortuosity, width and density, which are intrinsically related to the morphology of the new abnormal vessels. Moreover, NV occurs through ramification from existing vessels. Thus, the vessel number increases in terms NV, which is closely related to the branch number, where both properties are used in [5, 8, 10, 13, 15].

Although NV leads to the addition of new vessels, the vessel length has a weak correlation with NV. This results in several bifurcations rather than extending the length of initial ones. Correspondingly, the length feature is infrequently extracted. Furthermore, the retinal texture features are always correlated with the other morphological properties of NV.

We distinguish that few methods have extracted the four main NV properties. Among them, the work described in [10, 13] aimed to segment the neovascularized vessels, which relied on using higher computational complexity processing. Accordingly, they required higher execution times of 5.83 and 6.5 minutes, respectively. Similarly, the method put forward in [15] lied to extract 42 heavy processing features. Then, a feature selector was applied to identify 18 relevant ones to be used for classification. However, it was fail to outperform the detection performance of existing methods while the result required 8.74 seconds. As a consequence, increasing the size of feature set did not necessarily increase the detection performance.

Table 1. Targeted NV Properties in terms of NV detection methods

	NV properties	Vessel tortusoity	Vessel density	Vessel width	Number of Vessels	Number of Branches	Vessel length	Retina texture
Neovascularization screening	Hassan et al. (2012) [5]				X			X
	Agurto et al. (2012) [7]	X		X				
	Agurto et al. (2015)[12]	X	X	X				
	Gupta et al. (2017) [14]	X	X	X				X
	Yu et al. (2018)[15]	X	X	X	X	X	X	
	Huang et al. (2018)[9]	X						X
vessel segmentation	Goatman et al. (2011) [13]	X	X	X	X		X	X
	Akram et al. (2013) [10]	X	X	X	X			X
	Welikala et al. (2014) [8]	X	X		X			X
	SilKar et al. (2017) [11]	X	X					

3. Automated Method for PDR Detection

3.1. Approach principle

Our objective is to propose an automated method for detecting NV from retinal images captured by mobile devices. First of all, NV occurs on the OD before the whole retina. Moreover, the smartphone capture device has a limited field of view which does not allow modeling all retinal components. Therefore, to anticipate the detection of NV, our method ensures an early detection of NVD. Thus, the first step consists in automatically identifying and locating the OD.

The fundus images captured by smartphones are frequently blurred, noised, and have a non-balanced contrast. Subsequently, the OD will be enhanced through a pre-processing step. Since NV results in new vessels, we propose to segment the blood vessel tree belonging to the OD. In contrast to the existing methods for NV detection, we choose to deduce NV based on each vessel separately rather than using the whole vessel tree, in order to ensure higher accuracy and robustness.

Our challenge is to extract a set of features adequately reflecting the NVD without confusing with healthy images. Accordingly, our main contribution consists in extracting features related to the four morphological properties of NVD that are respectively the vessel tortuosity, the thinned width, the number of branches and the increased vessel density. In the last step, a classifier is utilized to classify whether the OD image contains NVD or not. Those processing steps are depicted in Fig.2, which are respectively described in the following sections.

3.2. Pre-processing

The method proposed in [28] insures locating the OD based on circularity and intensity through applying the radon transform. The method achieved a higher accurate performance, where an accuracy of 100% is performed to locate OD in the public DRIVE database. We note that this method is able to be configured with the aim of locating a sub-image having the same OD size. Thereafter, this method is extended to be provide a mobile computer aided system for OD detection [29]. The processing was

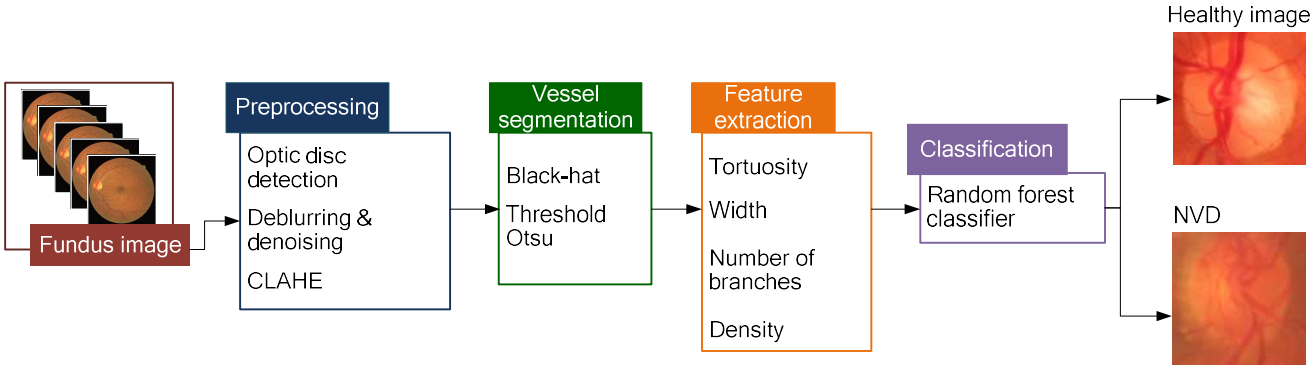

Fig.2 Diagram of our proposed method for NV detection

optimized to reduce complexity where the same detection accuracy is performed through 1.3 second in smartphone device. Therefore, the method proposed by [29] will be implemented which extract the OD sub-image in order to remove it from the fundus image.

Our objective is to segment the vessels that require the explicit modeling of vessels with respect to their background. Therefore, we extract the green channel as performed in several methods aiming for blood vessel tree segmentation [30–35], as illustrated in Fig.3(b1) and Fig.3(b2). Thereafter, due to the handheld aspect of the smartphone, the fundus images are always blurred and noised [20]. Thus, we apply the point spread function to the OD sub-image to enhance the image quality [30, 31] . Then, the Contrast Limited Adaptive Histogram Equalization (CLAHE) approach [36] is applied, where the pre-processed OD is shown in Fig.3(c1) and Fig.3(c2).

3.3. Vessel segmentation

NV entails abnormal thin vessels where a segmentation step remains crucial for NVD detection. The new vessels are less visible and have lower contrast than the normal ones, as illustrated in Fig. 3(a2). For this, we invert the gray level of the preprocessed image using the Black-hat morphological operator, as indicated in Fig.3(d1) and Fig.3(d2). Then, we segment the vessels through the "Otsu thresholding" [37, 38] where the final result is shown in Fig. 3(e1) and Fig.3(e2). NV consists in adding new vessels with specific forms. For this purpose, we extract each vessel through the detection contour processing, which is explained as a curve joining all continuous points having the same intensity [39].

3.4. Feature extraction

3.4.1. Tortuosity feature

Tortuosity is a morphological property of the retinal vessels. It can be defined as a non-smooth appearance of the vessel's course [15, 40]. NV increases the vascular tortuosity, as illustrated in Fig.1(b). This rise occurs as a result of the elevated blood pressure [41–43].

Several studies have demonstrated that the increased vessel tortuosity correlates with the severity of DR. The clinic-based study described in [44] studied the difference of tortuosity in relation with DR, where it was deduced that the arteriolar tortuosity grew with the rise in the DR severity. The work described in [45] indicated that the retinal vessels became tortuous either locally and/or over an extended area during retinal progression. Furthermore, these small vessels were more susceptible to become tortuous during the retinal NV stage. For this reason, we will extract a value that reflects the tortuosity to classify the OD sub-image as healthy or NVD.

Indeed, the more a vessel is tortuous, the greater the distance between the vessel extremities is. For this, we calculate the T_{vessel} tortuosity for each vessel, which is considered as the ratio between the vessel length L and the Euclidean distance D between the two vessel extremities [15, 46], as indicated in equation 1.

$$T_{vessel} = L/D \quad (1)$$

where length L is calculated using the modified "Riks" method [47]. For example, the vessel illustrated in Fig.4(a) has a healthy tortuosity where T_{vessel}=1.1. The neovascularized vessel shown in Fig.4(b) has high tortuosity where T_{vessel}= 2.

Fig.4 Vessels with different tortuosity: **(a)** low tortuous vessel, **(b)** high tortuous vessel

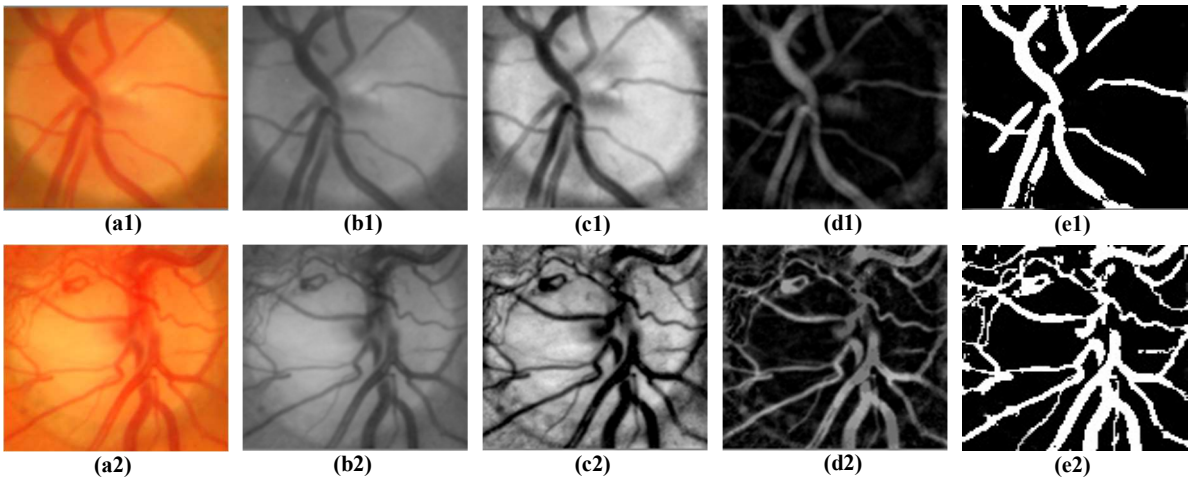

Fig.3 Pre-processing and Vessel segmentation: (a1) and (a2) healthy and NV OD image; (b1) and (b2) green channels of OD images; (c1) and (c2) pre-processed OD images ; (d1) and (d2) black-hat results of OD images ; (e1) and (e2) segmented vessel trees

The objective of this section is to generate a single feature related to the tortuosity of the whole vessel tree. The idea is to deduce the feature value from the T_{vessel} ones corresponding to all vessels belonging to the OD sub-image. In fact, a healthy image can contain vessels where most of them have a low tortuosity. For NV, several vessels with higher tortuosity are added. We proceed to illustrate the vessel distribution in terms of tortuosity, as presented in Fig.5. We deduce that the distribution of tortuosity for a healthy image is asymmetrical to the left, which indicates that small values of tortuosity correspond to 80% of the vessels, as shown in the Fig.5(a). In contrast, the distribution of tortuosity for an NVD image is asymmetrical to the right, which indicates that high tortuosity values are most frequent, where 80% of vessels have higher tortuosity values, as given in Fig. 5(b).

Our main idea consists in extracting a feature that reflects the distribution of vessel tortuosity. The mean of the vessels is an inadequate value for modeling tortuosity related to NV. For this, we employ the skewness which models the symmetrical degree of a distribution [48]. The skewness feature $Skewness_{tortuosity}$ reflects the tortuosity distribution, as indicated in equation 2.

$$Skewness_{tortuosity} = \frac{\sum_{i=1}^{N}(T_{vessel_i} - Moy)^3/N}{E^3} \quad (2)$$

where Moy represents the average of the tortuosities, E represents the standard deviation, N represents the total number of vessels, and T_{vessel} represents the tortuosity of a vessel. For instance, the tortuosity skewness of a healthy image is equal to 0.91, while it is equal to -0.35 for a neovascularized image.

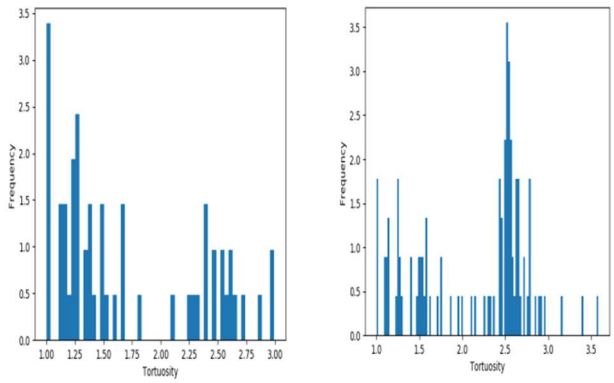

(a) (b)

Fig.5 Vessel distribution in terms of tortuosity: (**a**) healthy images, (**b**) neovascularized images

3.4.2. Width feature

NVD is characterized by the appearance of new vessels in the OD that have a thin width [7, 15] as represented in Fig.1(b). Multiple studies have primarily focused on the association between the retinal vascular width and the risk of DR where Wong et al. [49] showed that the DR were associated with narrowing arterioles. Additionally, Nguyen et al. [50] concluded that the retinal arteriolar caliber might be smaller with the increasing DR severity. For this purpose, we extract a feature that reflects the width in order to classify the image as healthy or NVD, as proceeded by the method in [10, 14, 15].

We determine the width L_{vessel} for each vessel in terms of pixels. The main processing idea consists in progressively thinning and quantifying the vessel width. Both steps are repeated until the vessel is disappears. Thus, the morphological "Erosion" transformation is iteratively applied, whose structuring $S_{element}$ element size is initialized at 1 and incremented by 1 at each iteration. The processing is turned off when the vessel sub-image becomes entirely black, as indicated in algorithm 1.

Algorithm 1 : vessel width computing

Input : a vessel
Output : L_{vessel} = h – 1
Begin
h←1
Repeat
apply Erosion (h*h)
h←h+1
Until (achieve black image)
End

Thereafter, the vessel width L_{vessel} is deduced in terms of the structuring element, as calculated in equation 3.

$$L_{vessel} = S_{element} - 1 \quad (3)$$

where $S_{element}$ represents the size of the structuring element. Figure 6 illustrates the vessel sub-images after each Erosion application. The structuring element size is increased from 1 to 8, whose vessel width L_{vessel} is equal to 7.

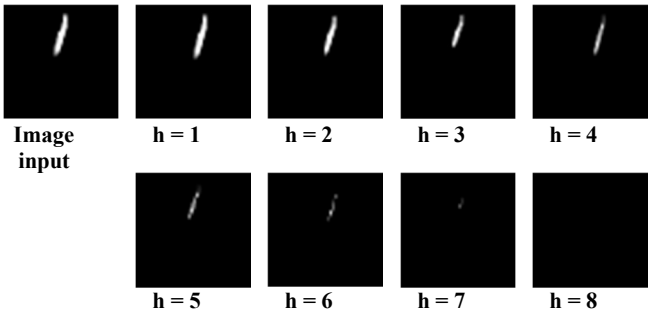

Fig.6 Erosion results in terms of structuring element sizes

The objective of this section is to generate a single feature deduced from all L_{vessel} width vessels of the OD sub-image. Therefore, we proceed to illustrate the vessel distribution in terms of width, as depicted in Fig.7. We deduce that the width distribution for a healthy image is asymmetrical to the right, where vessels having a width

above 2 represent 80% of all vessels, as shown in Fig.7(a). In contrast, the width distribution for an NVD image is asymmetrical to the left, where 80% of the vessels have a width value below 2.5, as provided in Fig.7(b). Our main idea consists in extracting a single width feature that reflects the distribution of the vessel width. Similarly, we compute a feature of width skewness $Skewness_{width}$ between all the vessels in order to model the width distribution, as indicated in equation 4.

$$Skewness_{width} = \frac{\sum_{i=1}^{N}(L_{vesse\ i} - Moy)^3/N}{E^3} \quad (4)$$

where Moy is the average width, E is the standard deviation, N represents the total number of vessels, and L_{vessel} represents the width of a vessel. For example, the width skewness of the healthy image is equal to -0.63, whereas it is equal to 0.49 for the NVD image.

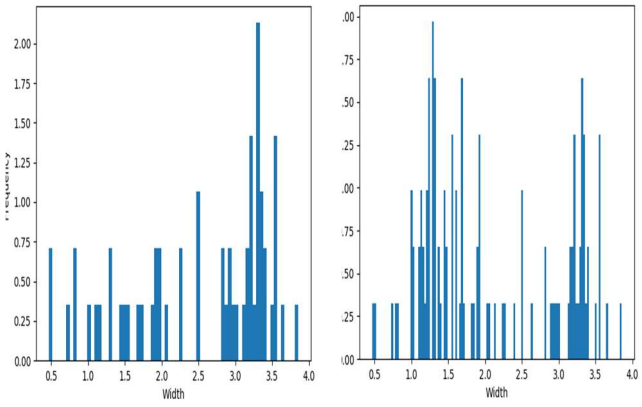

(a) **(b)**

Fig.7 Vessel distribution in terms of width: **(a)** healthy images, **(b)** neovascularized images

3.4.3. Number of branches

The retina contains four major arteries and veins that develop from the optic nerve head in order to propagate respectively in the inferior, nasal, superior and temporal regions. All other vessels fork from those major vessels through bifurcation nodes. When NV occurs, several new vessels appear especially in the OD. Consequently, a neovascularized OD has a high number of branches. As indicated in the work proposed by Pan et al. [3], the neovascularized vessel branch duplicated frequently in all directions, as depicted in Fig.1(b). For this purpose, we extract a value that reflects the number of branches in order to classify the image as healthy or NVD [15]. We want to identify the number of branches NB_{Br} for each vessel by applying the gift wrapping Algorithm. This latter allows computing the convex hull [51] that generates a polygon whose encompasses the vessel [52], as shown in the vessel modeled in Fig.8. As a result, the number of branches of the vessel is deduced, which corresponds to the number of the polygon sides. Thereafter, we deduce bifurcation by computing the total number of branches $NB_{Br_{total}}$ of all vessels, as calculated in equation 5.

$$NB_{Br_{total}} = \sum_{i=1}^{N} NB_{Br\ i} \quad (5)$$

where NB_{Br} represents the number of branches of a vessel, and N represents the total number of vessels. For instance, the number of branches for the healthy OD of Fig.3(a1) is equal to $NB_{Br_{total}} = 135$, while it is equal to $NB_{Br_{total}} = 227$ for the neovascularized OD illustrated in Fig.3(a2).

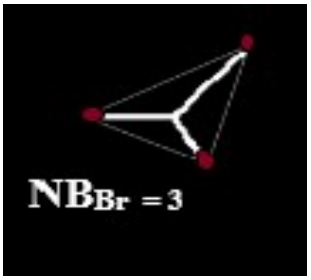

Fig.8 Number of branches computing

3.4.4. Blood vessel density

NV is characterized by the appearance of new vessels due to a significant lack of oxygen in the retinal capillaries [5]. The new vessels are denser than the normal blood vessels [8, 10, 13]. Therefore, we extract a value that reflects the density of blood vessels in order to classify the image as healthy or NVD. For this purpose, we calculate the density of all blood vessels D_{vessel} in the OD, which is considered to be the ratio between [10, 11] the vessel area and the OD area, as indicated in equation 6.

$$D_{vessel} = {}^{x1}/_{x2} \quad (6)$$

where x1 is the number of all vessel pixels, and x2 is the total number of OD pixels. For the healthy OD shown in Fig.1(a), the vessel density is equal to $D_{vessel} = 0.20$. In contrast, the neovascularized OD in Fig.1(b) has a vessel density equal to $D_{vessel} = 0.27$.

3.5. Classification

The classifier must provide a higher performant classification based on the extracted features. This performance is to be ensured even when using a reduced size of dataset for training. Moreover, the classifier should be characterized by a lower complexity in order to be adequate for a mobile implementation [21, 53]. For this purpose, we select classifiers that attest those criteria, which are the SVM and the RF classifiers. For each classifier, the provided results depend on the manner in which their parameters are initialized. Therefore, we describe both classifiers in the following sub-sections where we focus on their parameters.

Thereafter, we perform an experimental study, as detailed in section 5.2, where each classifier is employed with different parameters, as done in [X, Y]. Thereupon, the classifier achieving the better detection performances is identified to be integrated on our proposed method.

3.5.1. SVM

The SVM is an automatic learning algorithm used for data classification, which is widely used for binary classification [X]. The principal objective of SVM is to determine an optimal hyperplane that separates the training data into classes, by maximizing the geometric margin between each other [54–56]. Many related works [12, 13, 15] used the SVM classifier to detect the NVD where optimal performances have been achieved. The hyperplane generation depends of the used kernel that can be polynomial, Radial Basis Function (RBF) and sigmoid function [57]. All kernels have common parameter called the cost C and the slope gamma γ. The SVM classifier provided adequate performance when a reduced training dataset is used. Moreover, the SVM complexity is equal to $\boldsymbol{\max(data \times vec), data^2)}$ [58, 59], where $\boldsymbol{data}$ is the number of images used on the training process and $\boldsymbol{d}$ is feature set size, hence requiring a constant execution time.

3.5.2. RF

The RF [60] is an ensemble of decision tree classifiers. Each tree is formed independently of the other using a randomly selected subset of a training set. The forest corresponds to a collection of trees where the classification result is decided whether by weighted voting or majority voting. The RF is widely used in solving classification problems [61–64], particularly for classifying DR retinal images [65, 66, X, X].

The RF has four main parameters [67] which are the number of trees in the forest, the maximum depth of the tree, the number of features considered for splitting a node and the size of the training set. The model variance of a RF classifier decreases with respect to the rise of tree number, while maintaining the same bias [68]. The RF is characterized by a low number of control where the complexity of the prediction phase is $\boldsymbol{O(set \times tree)}$ where $\boldsymbol{set}$ is the feature set size and $\boldsymbol{tree}$ is the number of trees [69].

4. Implementation of the MAS-PDR

Android is an open source operating system for mobile devices, published by Google under the Apache license [70]. The implementation was made for Android smartphones using the Android software development kit. We use the JAVA language to write a program in Android Studio. The processing related to image processing and classification is coded using The "Open Source Computer Vision (OpenCV)" multiplatform library, developed by Intel. It focuses mainly on image processing and computer vision [29, 39] and provides rapid and efficient data structures and algorithms that can be used for complex real-time applications [52]. It offers more than 2500 optimized image processing functions written in C / C ++ language [29]. To compile and incorporate the functions written in C / C ++ language, the Android native development kit is installed and configured in our project.

The PDR screening method is implemented using Android Studio 3.5 with a PC powered by Intel Core i3, CPU 2 GHz and 4GO RAM. A graphical user interface is developed to allow using the method as an Android app, as shown in Fig.9. When the application is launched, the "Fundus Image Selection" button allows opening the smartphone gallery in order to select the fundus image. Thereafter, the processing proposed in [29] is processed to locate and display the OD in the graphical interface. The "Neovascularization Detection" button leads to run the suggested method and post a message to the user indicating the screening result.

5. Experimental Results

In this section, we aim to evaluate the proposed method for NVD detection, in terms of detection performance and execution time. For this purpose, the experiment consists in identifying the dataset and the detection metrics used for evaluation, as depicted in the first sub-section. In the second sub-section, the NVD detection performances of the suggested method are extracted and compared with the different existing techniques. Then, the evaluation of the robustness of the method with images captured by a smartphone is presented in the third sub-section. Moreover, the execution time of our method is evaluated and compared to some related work in the last sub-section.

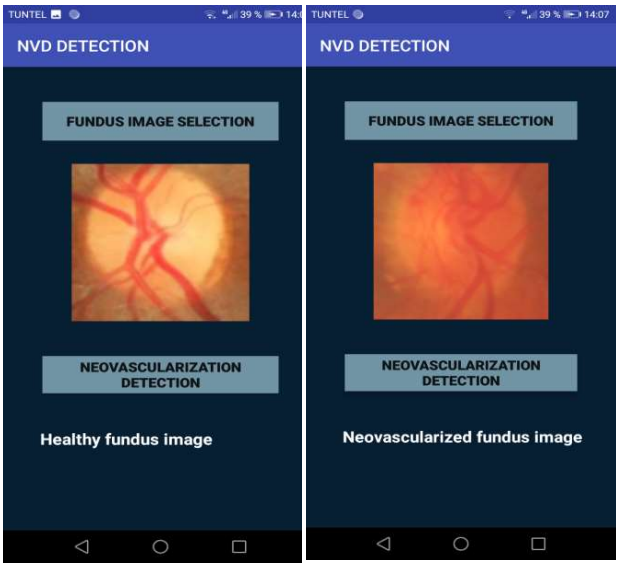

(a) **(b)**

Fig.9 Smartphone graphical interface: **(a)** Healthy image detection, **(b)** NV detection

5.1. Fundus image dataset

Based on the state of the art study presented in section 2, the NV detection methods are always evaluated using dataset where fundus images are collected from different databases since no one contains sufficient NVD fundus images. For this purpose, we construct a database of 306 images captured by retinograph, which contains 106 NVD images and 200 healthy images. To ensure a reliable evaluation, 30% of fundus images are assigned as NVD. The image resources used in this document are collected from eight publically accessible databases, where the number of images is detailed in Table 2.

Table 2. Fundus images selected from publically Databases

Database	Number of healthy images	Number of NVD images
DRIVE	15	0
DIARETDB1	20	3
HRF	15	3
DIARETDB0	20	7
Messidor	40	17
Kaggle	0	10
STARE	17	3
EyePACS	73	63

The collected fundus images have different resolution, such as the DRIVE, STARE and MESSIDOR datasets where the sizes are respectively 768×584, 700×605 and exceed 1440×960. This divergence leads to different OD size where the radius ranges from 80 to 200 pixels. In order to unify the processing, the images are resized to have an OD radius of 100 pixels.

5.2. Evaluation approach

To evaluate the performance of our method, we use three parameters for the evaluation purpose which are sensitivity (Sens), specificity (Spec) and accuracy (ACC) given in equations (7) – (9), respectively.

$$\text{Sensitivity} = \frac{TP}{TP+FN} \quad (7)$$

$$\text{Specificity} = \frac{TN}{TN+FP} \quad (8)$$

$$\text{Accuracy} = \frac{TP+TN}{TP+TN+FP+F} \quad (9)$$

where TP, TN, FP and FN are respectively the True Positive, the True Negative, the False Positive and the False Negative detected images.

To ensure credibility whether for chosen classifiers or for deduced performances, we apply a 10-cross validation. The process consists in splitting the dataset where 70% of the data are used for training and 30% for testing. The repartition is randomly done ten times to provide different sets whether dedicated for training or testing.

5.3. Feature evaluation

Our main contribution consists at adequately choosing features in order to reflect the NV properties. For this purpose, we proceed to evaluate the features ability to distinguish between healthy and neovascularized OD. For each feature, we model graphically all extracted values as points in a 2D Cartesian space, where the vertical axis expands the value gap, as shown in Fig.10. The feature values that correspond to healthy and neovascularized images are modeled respectively with blue and orange colors.

We deduce that values of each class are apparently clustered, despite the important size of the dataset. This evaluation attests the meaningful of the chosen features. However, the clusters are not linearly separable, where their value gaps are overlapped. The value crossover is obvious where reflected properties are already outlined in a healthy OD. Therefore, a screening cannot be performed using any feature separately.

5.4. Classification evaluation

In this section, we choose the adequate classifier and its configuration that allows achieving a higher detection performance. Within this objective, we extract the features of all fundus image datasets. Thereafter, the SVM and random forest classifiers are trained with different configuration, using the same feature set.

For the SVM, we experimentally test the classifier with three different kernels that are respectively the sigmoid, the RBF and the polynomial, where the achieved accuracy, sensitivity and specificity are indicated in the three first

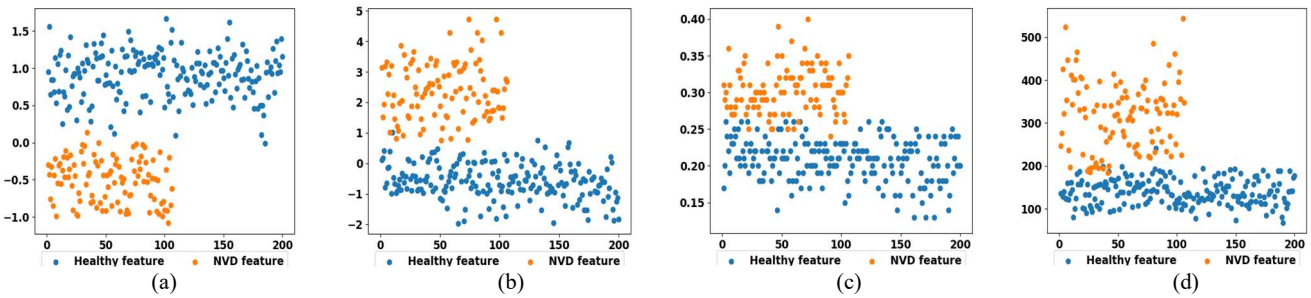

Fig.10 distribution of feature values: (a) tortuosity, (b) width; (c) density: (d) number of branches

Table 3. Performance comparison between SVM and RF classifiers

Classifier	SVM			Random forest		
	Sigmoid	RBF	Poly	depth = 6	8	10
Acc (%)	94.02	97.39	98.47	98.69	98.69	98.69
Sens (%)	91.30	95.70	97.88	97.73	97.73	97.73
Spec (%)	95.50	98.25	98.75	99.12	99.12	99.12

columns of Table 3. We note that the C, γ and d parameters are selected using the grid search method, which is widely used and considered by the most accurate optimization technique [54]. For the random forest, the feature number is fixed to the maximal value, as we have only four ones. In addition, the tree number is fixed to 500. The tree depth is varied following the above values {6, 8, 10} where their results are illustrated in the three last columns of Table 3. We deduce that using the RF classifier allows achieving 98.69% accuracy, 97.73% sensitivity and a 99.12% specificity, for any depth suggested. That is why, the RF classifier with tree depth equal to 6 is chosen for our proposed method. We use the box plots to present the performance of these experiments, as shown in Fig.11(a). These box plots demonstrate high performances in terms of accuracy, sensitivity and specificity. Moreover, those higher performances are guaranteed whatever the dataset used for training testing. This aspect proves the performance of our method or when using new captured fundus images, which corresponds to clinical utilization.

5.5. Evaluation with respect to existing methods

We evaluate our method with respect to the existing ones in terms of detection performances and number of extracted features, as illustrated in Table 4. Our proposed method registers the highest accuracy and specificity compared to all NV and NVD detection methods. Moreover, our method achieves better sensitivity compared to the NVD method presented by [7, 13, 15], even we proceeded with a 10-cross validation.

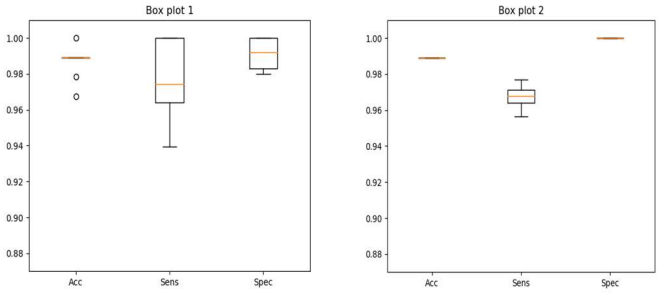

(a) (b)

Fig.11 Performance visualization using box plots: (**a**) initial fundus images dataset, (**b**) motion blurred fundus image dataset

This performance is caused by the targeted NV properties which present adequate and complementary set for the NV modeling. We note that our dataset has greater or similar size than the ones used in [10, 13, 15]. While the accuracy of the method described in [13] is not provided, the detection performance of our method outperforms the methods proposed in [10] and [15]. Moreover, the achieved sensitivity and specificity obviously exceed the ones registered the three methods. This result is due to the meaningful processing features that we put forward.

5.6. Evaluation of the method robustness with respect to smartphone captured images

In this section, we evaluate the suggested method with respect to the degraded quality of fundus images captured by smartphones. We notice that no public database of

Table 4. Comparison of NV detection methods

	Method	Dataset	Number of Feature	Acc	Sens	Spec
Neovascularization screening	Hassan et al. (2012) [5]	11 NV + 302 Neg	2	_	93.90%	89.40%
	Agurto et al. (2012) [7]	27 NVD + 30 Neg	41		96%	83%
	Agurto et al. (2015)[12]	100 NVD + 200 Neg	1248	88%	78%	94%
	Gupta et al. (2017) [14]	100 NV + 679 Neg	525	_	92 .2%	83%
	Yu et al. (2018)[15]	134 NVD + 290 Neg	42	95.23 %	92.9%	96.30 %
	Huang et al. (2018)[9]	42 images	5	89.20%	_	_
vessel segmentation	Goatman et al. (2011) [13]	38 NVD + 71 Neg	15	_	84.2%	85.90%
	Akram et al. (2013) [10]	63 NV + 451 Neg	10	95%	96.5%	93%
	Welikala et al. (2014) [8]	20 NV + 40 Neg	4	_	100%	90%
	SilKar et al. (2017) [11]	26 NV + 1368 Neg	2	97.49%	97.45%	96.03%
	Proposed method	**106 NVD + 200 Neg**	**4**	**98.69 %**	**97.73%**	**99.12 %**

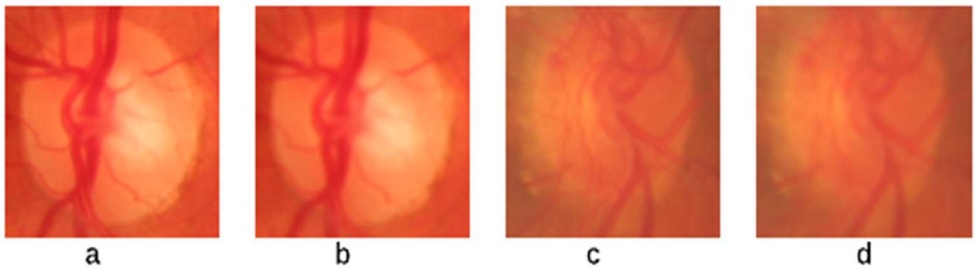

Fig.12 original and blurred fundus images: **(a)** and (c) fundus images, **(b)** and **(d)** fundus images after applying motion blur filter

fundus images captured with smartphones. In fact, a smartphone-captured fundus image is blurred and noised due to the handheld holding of smartphones. Therefore, the main idea is to apply a data augmentation for classical fundus image where the processing simulates the blurs and noises. For this purpose, we use the same database of fundus images described in section 5.1 where we apply the motion blur filter with a kernel of 2x2 size for each image. The ODs depicted in Fig.12(b) and Fig.12(d) are provided after applying the mentioned filter to the ODs shown respectively in Fig.12(a) and Fig.12(c). Then, the same 10-cross evaluation experiment is repeated where average accuracy of 98.91%, sensitivity of 96.75% and specificity of 100% are registered. The different performances of each cross-validation set are modeled through the box plots illustrated in Fig.11(b). The merged plot sizes reflect the sustainability of the method whatever the degraded images used for training or for testing. We deduce that the detection performances remain higher even with a degraded image quality. Accordingly, the result proves the robustness of our method and confirms its ability to be employed on a mobile MAS system for PDR.

5.7. Computational performance of MAS-PDR

5.7.1. *Complexity analysis*

The point spread function, the CLAHE algorithm and the black-hat filter proceed to browse all pixels of the OD sub-image in order to provide the new pixel values. therefore, each processing requires $(n \times n)$ to be done [71], where $(n \times n)$ is the size of OD sub-image. The Otsu thresholding consists in comparing and generating a pixel value, which is repeated $(n \times n)$ times [72]. Similarly, the extraction of each vessel requires $(n \times n)$ instructions [73].

The complexities of the RIKs method, the Erosion morphological operator and the convex hull algorithm are equal to $(n \times n)$. Those processing are performed v times, where v is the number of vessels. Moreover, the vessel density requires scanning all pixels and hence performed in $(n \times n)$. Finally, the RF classifier leads to browse 500 trees composed by 4 features and hence requiring constant complexity to be processed. Consequently, the whole method complexity is equal to $O(n \times n \times v)$, where $(n \times n)$ is the size of OD sub-image ad v is the number of vessels.

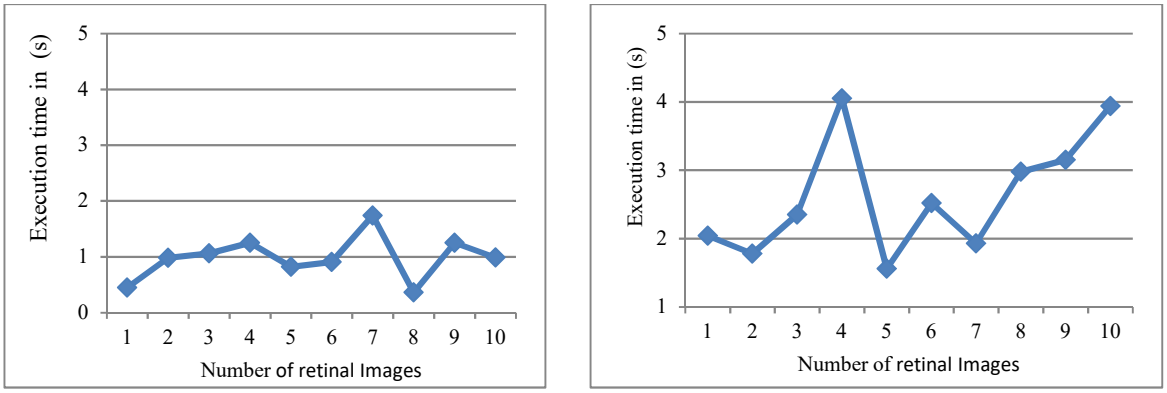

(a) **(b)**

Fig .13 Execution times of NV detection: **(a)** healthy images, **(b)** NV images

Table 5. Execution times for NV detection methods

Method	Execution time
Goatman et al. (2011) [13]	5.83 min
Hassan et al. (2012) [5]	7.43 min
Akram et al. (2013) [10]	6.5 min
SilKar et al. (2017) [11]	2.25 min
Yu et al. (2018)[15]	8.74 s
Proposed method	**0.9 s (healthy image)** **2.63s (NV image)**

5.7.2. Execution time evaluation

In this section, we proceed to evaluate the execution time performance of our proposed method. For this purpose, the MAS-PDR app is implemented in the SAMSUNG S5 smartphone, which can be combined with the optical lens D-EYE. Thereafter, we choose randomly 20 fundus images which are partitioned into 10 healthy and 10 NVD, where execution times are respectively shown in Fig.13(a), Fig.13(b). We deduce that the average execution time of healthy images is about 0.9 seconds, while it is equal to 2.63 seconds for the NVD images. In fact, our method is based on extracting retinal vessels and then exploring each segmented vessel where NVD leads to increasing the vessel number. As an example, the average number of vessels in healthy OD is about 40, while it is equal to 100 in the case of NVD images. This difference explains the gap of execution times among healthy and NVD fundus images.

Thereafter, we compare the execution times of our method to the existing NVD detection methods, where values are shown in Table 5. We indicate that only methods providing the execution times are considered. We deduce that our method achieves better execution time than all reported methods, despite that our method is executed on smartphone device while others were implemented in desktops. For instance, the detection requires more than 2 minutes when using the methods proposed in [5, 10, 11, 13]. Particularly, our method provides a faster result than the one suggested in [15]. This result is caused by the optimal feature set that we suggested which is limited on four features with a low computational complexity. Accordingly, the computational performance is perfectly adequate to the clinical employment of MAS-PDR.

6. Conclusion

In this paper, an automated method for NV detection has been proposed to provide the early detection of NV. This method was implemented into smartphones to provide a MAS system for PDR. This processing consists in detecting and enhancing the OD. Thereafter, the vessel tree is segmented where each vessel is extracted separately. Our main contribution consists in providing four adequate features that are exactly related to the morphologies of the neovascularized vessels. The provided features are given to a RF classifier to ensure higher performance detection with 98.69% accuracy. We have also evaluated the robustness of the method by applying the motion blur to the fundus image datasets, where a higher performance is maintained with 98.91% accuracy.

In our future work, we aim to propose a MAS system for DR severity while guaranteeing the same accuracy and robustness. In addition, we will provide real-time detection which can be performed into a retinal capture video stream. Furthermore, other work must be focused into generating a new database dedicated for smartphone-captured fundus images.

References

1. Boittiaux, P. (2016, November 14). L'essor du diabète dans le monde. Retrieved from https://fr.statista.com/infographie/6699/lessor-du-diabete-dans-le-monde/
2. Sabanayagam, C., Banu, R., Chee, M. L., Lee, R., Wang, Y. X., Tan, G., … Wong, T. Y. (2019). Incidence and progression of diabetic retinopathy: a systematic review. The Lancet Diabetes & Endocrinology, 7(2), 140–149.
3. Pan, J., Chen, D., Yang, X., Zou, R., Zhao, K., Cheng, D., … Chen, F. (2018). Characteristics of Neovascularization in Early Stages of Proliferative Diabetic Retinopathy by Optical Coherence Tomography Angiography. American Journal of Ophthalmology, 192, 146–156.
4. Ting, D. S. W., Cheung, G. C. M., & Wong, T. Y. (2016). Diabetic retinopathy: global prevalence, major risk factors, screening practices and public health challenges: a review: Global burden of diabetic eye diseases. Clinical & Experimental Ophthalmology, 44(4), 260–277.
5. Hassan, S. S. A., Bong, D. B. L., & Premsenthil, M. (2012). Detection of Neovascularization in Diabetic Retinopathy. Journal of Digital Imaging, 25(3), 437–444.
6. Chalakkal, R. J., Abdulla, W. H., & Hong, S. C. (2020). Fundus retinal image analyses for screening and diagnosing diabetic retinopathy, macular edema, and glaucoma disorders. In Diabetes and Fundus OCT (pp. 59–111). Elsevier.
7. Agurto, C., Honggang Yu, Murray, V., Pattichis, M. S., Barriga, S., Bauman, W., & Soliz, P. (2012). Detection of neovascularization in the optic disc using an AM-FM representation, granulometry, and vessel segmentation. In 2012 Annual International Conference of the IEEE Engineering in Medicine and Biology Society (pp. 4946–4949). Presented at the 2012 34th Annual International Conference of the IEEE Engineering in Medicine and Biology Society (EMBC), San Diego, CA: IEEE.
8. Welikala, R. A., Dehmeshki, J., Hoppe, A., Tah, V., Mann, S., Williamson, T. H., & Barman, S. A. (2014). Automated detection of proliferative diabetic retinopathy using a modified line operator and dual classification. Computer Methods and Programs in Biomedicine, 114(3), 247–261.
9. Huang, H., Ma, H., JW van Triest, H., Wei, Y., & Qian, W. (2018). Automatic detection of neovascularization in retinal images using extreme learning machine. Neurocomputing, 277, 218–227.
10. Usman Akram, M., Khalid, S., Tariq, A., & Younus Javed, M. (2013). Detection of neovascularization in retinal images using

multivariate m-Mediods based classifier. Computerized Medical Imaging and Graphics, 37(5–6), 346–357.
11. SilKar, S., & Maity, S. P. (2017). Detection of neovascularization in retinal images using mutual information maximization. Computers & Electrical Engineering, 62, 194–208.
12. Agurto, C., Yu, H., Murray, V., Pattichis, M. S., Nemeth, S., Barriga, S., & Soliz, P. (2015). A multiscale decomposition approach to detect abnormal vasculature in the optic disc. Computerized Medical Imaging and Graphics, 43, 137–149.
13. Goatman, K. A., Fleming, A. D., Philip, S., Williams, G. J., Olson, J. A., & Sharp, P. F. (2011). Detection of New Vessels on the Optic Disc Using Retinal Photographs. IEEE Transactions on Medical Imaging, 30(4), 972–979.
14. Gupta, G., Kulasekaran, S., Ram, K., Joshi, N., Sivaprakasam, M., & Gandhi, R. (2017). Local characterization of neovascularization and identification of proliferative diabetic retinopathy in retinal fundus images. Computerized Medical Imaging and Graphics, 55, 124–132.
15. Yu, S., Xiao, D., & Kanagasingam, Y. (2018). Machine Learning Based Automatic Neovascularization Detection on Optic Disc Region. IEEE Journal of Biomedical and Health Informatics, 22(3), 886–894.
16. Number of smartphone users worldwide from 2016 to 2021. (2017, October). Retrieved from https://www.statista.com/statistics/330695/number-of-smartphone-users-worldwide/
17. Wu, A. R., Fouzdar-Jain, S., & Suh, D. W. (2018). Comparison Study of Funduscopic Examination Using a Smartphone-Based Digital Ophthalmoscope and the Direct Ophthalmoscope. Journal of Pediatric Ophthalmology & Strabismus, 55(3), 201–206.
18. Russo, A., Morescalchi, F., Costagliola, C., Delcassi, L., & Semeraro, F. (2015). A Novel Device to Exploit the Smartphone Camera for Fundus Photography. Journal of Ophthalmology, 2015, 1–5.
19. Panwar, N., Huang, P., Lee, J., Keane, P. A., Chuan, T. S., Richhariya, A., … Agrawal, R. (2016). Fundus Photography in the 21st Century—A Review of Recent Technological Advances and Their Implications for Worldwide Healthcare. Telemedicine and e-Health, 22(3), 198–208.
20. Akil, M., & Elloumi, Y. (2019). Detection of retinal abnormalities using smartphone-captured fundus images: a survey. In N. Kehtarnavaz & M. F. Carlsohn (Eds.), Real-Time Image Processing and Deep Learning 2019 (p. 21). Presented at the Real-Time Image Processing and Deep Learning 2019, Baltimore, United States: SPIE.
21. Prasanna, P., Jain, S., Bhagat, N., & Madabhushi, A. (2013). Decision Support System for Detection of Diabetic Retinopathy Using Smartphones. In Proceedings of the ICTs for improving Patients Rehabilitation Research Techniques. Presented at the ICTs for improving Patients Rehabilitation Research Techniques, Venice, Italy: IEEE.
22. Bourouis, A., Feham, M., Hossain, M. A., & Zhang, L. (2014). An intelligent mobile based decision support system for retinal disease diagnosis. Decision Support Systems, 59, 341–350.
23. Monjur, M., Hoque, I., Hashem, T., Rakib, A., Kim, J., & Ahamed, S. iqbal. (2019). Smartphone Based Fundus Camera for the Diagnosis of Retinal Diseases. In IEEE/ACM CHASE (p. 13). United States. Retrieved from https://www.researchgate.net/publication/335292278
24. Majumder, S., Elloumi, Y., Akil, M., Kachouri, R., & Kehtarnavaz, N. (2020). A deep learning-based smartphone app for real-time detection of five stages of diabetic retinopathy. In N. Kehtarnavaz & M. F. Carlsohn (Eds.), Real-Time Image Processing and Deep Learning 2020 (p. 5). Presented at the Real-Time Image Processing and Deep Learning 2020, Online Only, United States: SPIE.
25. Martins, J., Cardoso, J. S., & Soares, F. (2020). Offline computer-aided diagnosis for Glaucoma detection using fundus images targeted at mobile devices. Computer Methods and Programs in Biomedicine, 192, 105341.
26. Guo, F., Mai, Y., Zhao, X., Duan, X., Fan, Z., Zou, B., & Xie, B. (2018). Yanbao: A Mobile App Using the Measurement of Clinical Parameters for Glaucoma Screening. IEEE Access, 6, 77414–77428.
27. Huang, H., Ma, H., & Qian, W. (2019). Automatic Parallel Detection of Neovascularization from Retinal Images Using Ensemble of Extreme Learning Machine *. In 2019 41st Annual International Conference of the IEEE Engineering in Medicine and Biology Society (EMBC) (pp. 4712–4716). Presented at the 2019 41st Annual International Conference of the IEEE Engineering in Medicine & Biology Society (EMBC), Berlin, Germany: IEEE.
28. Pourreza-Shahri, R., Tavakoli, M., & Kehtarnavaz, N. (2014). Computationally efficient optic nerve head detection in retinal fundus images. Biomedical Signal Processing and Control, 11, 63–73.
29. Elloumi, Y., Akil, M., & Kehtarnavaz, N. (2018). A mobile computer aided system for optic nerve head detection. Computer Methods and Programs in Biomedicine, 162, 139–148.
30. Deshpande, A. M., & Patnaik, S. (2014). Single image motion deblurring: An accurate PSF estimation and ringing reduction. Optik, 125(14), 3612–3618.
31. Cai, J.-F., Ji, H., Liu, C., & Shen, Z. (2009). Blind motion deblurring using multiple images. Journal of Computational Physics, 228(14), 5057–5071.
32. Aras, R. A., Lestari, T., Nugroho, H. A., & Ardiyanto, I. (2016). Segmentation of retinal blood vessels for detection of diabetic retinopathy: A review. COMMUNICATIONS IN SCIENCE AND TECHNOLOGY, pp. 33–41.
33. Dash, J., & Bhoi, N. (2017). A thresholding based technique to extract retinal blood vessels from fundus images. Future Computing and Informatics Journal, 2(2), 103–109.
34. Moccia, S., De Momi, E., El Hadji, S., & Mattos, L. S. (2018). Blood vessel segmentation algorithms — Review of methods, datasets and evaluation metrics. Computer Methods and Programs in Biomedicine, 158, 71–91.
35. Akil, M., & Elloumi, Y. (2018). Computationally efficient blood vessels segmentation in fundus image on shared memory parallel machines. In N. Kehtarnavaz & M. F. Carlsohn (Eds.), Real-Time Image and Video Processing 2018 (p. 7). Presented at the Real-Time Image and Video Processing 2018, Orlando, United States: SPIE.
36. Chalakkal, R. J., & Abdulla, W. (2017). Automatic segmentation of retinal vasculature. In 2017 IEEE International Conference on Acoustics, Speech and Signal Processing (ICASSP) (pp. 886–890). Presented at the 2017 IEEE International Conference on Acoustics, Speech and Signal Processing (ICASSP), New Orleans, LA: IEEE.
37. Muramatsu, C., Nakagawa, T., Sawada, A., Hatanaka, Y., Hara, T., Yamamoto, T., & Fujita, H. (2010). Automated segmentation of optic disc region on retinal fundus photographs: comparison of contour modeling and pixel

classification methods. Comput. Methods Programs Biomed, 23–32.
38. Nakagawa, T., Hayashi, Y., Hatanaka, Y., Aoyama, A., Mizukusa, Y., Fujita, A., & Kakogawa, M. (2006). Recognition of optic nerve head using blood-vessel-erased image and its application to production of simulated stereogram in computer-aided diagnosis system for retinal images. IEICE Trans. Inf. Syst.
39. Kumari, S., Gupta, L., & Gupta, P. (2017). Automatic License Plate Recognition Using OpenCV and Neural Network. International Journal of Computer Science Trends and Technology (IJCST), 5.
40. Grisan, E., Foracchia, M., & Ruggeri, A. (2008). A Novel Method for the Automatic Grading of Retinal Vessel Tortuosity. IEEE Transactions on Medical Imaging, 27(3), 310–319.
41. Cheung, C. Y., Zheng, Y., Hsu, W., Lee, M. L., Lau, Q. P., Mitchell, P., … Wong, T. Y. (2011). Retinal Vascular Tortuosity, Blood Pressure, and Cardiovascular Risk Factors. Ophthalmology, 118(5), 812–818.
42. Paul, V. (2018, December 27). Significance of Asymmetric Retinal Vasculature Tortuosity - Report of 10 Consecutive Cases, p. 5.
43. Kubicek, J., Timkovic, J., Krestanova, A., Augustynek, M., Penhaker, M., & Bryjova, I. (2018). Morphological Segmentation of Retinal Blood Vessels and Consequent Tortuosity Extraction. journal of telecommunication electronic and computer engineering, 10(1–4).
44. Sasongko, M. B., Wong, T. Y., Nguyen, T. T., Cheung, C. Y., Shaw, J. E., & Wang, J. J. (2011). Retinal vascular tortuosity in persons with diabetes and diabetic retinopathy. Diabetologia, 54(9), 2409–2416.
45. Zhu, S., Liu, H., Du, R., Annick, D. S., Chen, S., & Qian, W. (2020). Tortuosity of Retinal Main and Branching Arterioles, Venules in Patients With Type 2 Diabetes and Diabetic Retinopathy in China. IEEE Access, 8, 6201–6208.
46. Mustafa, N. B. A., Zaki, W. M. D. W., & Hussain, A. (2015). A review on the diabetic retinopathy assessment based on retinal vascular tortuosity. In 2015 IEEE 11th International Colloquium on Signal Processing & Its Applications (CSPA) (pp. 127–130). Presented at the 2015 IEEE 11th International Colloquium on Signal Processing & Its Applications (CSPA), Kuala Lumpur, Malaysia: IEEE.
47. Riks, E. (1979). An incremental approach to the solution of snapping and buckling problems. International Journal of Solids and Structures, 15(7), 529–551.
48. Mardia, K. V. (1970). Measures of multivariate skewness and kurtosis with applications. Biometrika, 57(3), 519–530.
49. Wong, T. Y. (2005). Retinal Arteriolar Narrowing, Hypertension, and Subsequent Risk of Diabetes Mellitus. Archives of Internal Medicine, 165(9), 1060.
50. Nguyen, T. T., Wang, J. J., Islam, F. M. A., Mitchell, P., Tapp, R. J., Zimmet, P. Z., … Wong, T. Y. (2008). Retinal Arteriolar Narrowing Predicts Incidence of Diabetes: The Australian Diabetes, Obesity and Lifestyle (AusDiab) Study. Diabetes, 57(3), 536–539.
51. Sharif, M. (n.d.). A new Approach to Compute Convex Hull. Innovative Systems Design and Engineering, 2, 8.
52. Amiraj, D., & Honrao, V. (2013). Implementation of Hand Detection based Techniques fo Human Computer Interaction. International Journal of Computer Applications, 72.
53. Saki, F., Sehgal, A., Panahi, I., & Kehtarnavaz, N. (2016). Smartphone-based real-time classification of noise signals using subband features and random forest classifier. In 2016 IEEE International Conference on Acoustics, Speech and Signal Processing (ICASSP) (pp. 2204–2208). Presented at the 2016 IEEE International Conference on Acoustics, Speech and Signal Processing (ICASSP), Shanghai: IEEE.
54. Kavzoglu, T., & Colkesen, I. (2009). A kernel functions analysis for support vector machines for land cover classification. International Journal of Applied Earth Observation and Geoinformation, 11(5), 352–359.
55. Abe, S. (2010). Support Vector Machines for Pattern Classification. London: Springer London.
56. Ahmed, M., Naser Mahmood, A., & Hu, J. (2016). A survey of network anomaly detection techniques. Journal of Network and Computer Applications, 60, 19–31.
57. Karatzoglou, A., Meyer, D., & Hornik, K. (2006). Support Vector Machines in R. Journal of Statistical Software, 15(9).
58. Ayinala, M., & Parhi, K. K. (2012). Low complexity algorithm for seizure prediction using Adaboost. In 2012 Annual International Conference of the IEEE Engineering in Medicine and Biology Society (pp. 1061–1064). Presented at the 2012 34th Annual International Conference of the IEEE Engineering in Medicine and Biology Society (EMBC), San Diego, CA: IEEE.
59. Madroñal, D., Lazcano, R., Salvador, R., Fabelo, H., Ortega, S., Callico, G. M., … Sanz, C. (2017). SVM-based real-time hyperspectral image classifier on a manycore architecture. Journal of Systems Architecture, 80, 30–40.
60. Breiman, L. (2001). Random Forests. Machine Learning, 45(1), 5–32.
61. Zhang, Y., Wei, S., Zhang, L., & Liu, C. (2019). Comparing the Performance of Random Forest, SVM and Their Variants for ECG Quality Assessment Combined with Nonlinear Features. Journal of Medical and Biological Engineering, 39(3), 381–392.
62. Abdulhay, E., Alafeef, M., Abdelhay, A., & Al-Bashir, A. (2017). Classification of Normal, Ictal and Inter-ictal EEG via Direct Quadrature and Random Forest Tree. Journal of Medical and Biological Engineering, 37(6), 843–857.
63. Lin, C.-Y., Yi, T., Gao, Y.-Z., Zhou, J.-H., & Huang, Q.-H. (2017). Early Detection and Assessment of Liver Fibrosis by using Ultrasound RF Time Series. Journal of Medical and Biological Engineering, 37(5), 717–729.
64. Ayata, D., Yaslan, Y., & Kamasak, M. E. (2020). Emotion Recognition from Multimodal Physiological Signals for Emotion Aware Healthcare Systems. Journal of Medical and Biological Engineering, 40(2), 149–157.
65. Casanova, R., Saldana, S., Chew, E. Y., Danis, R. P., Greven, C. M., & Ambrosius, W. T. (2014). Application of Random Forests Methods to Diabetic Retinopathy Classification Analyses. PLoS ONE, 9(6), e98587.
66. Roychowdhury, A., & Banerjee, S. (2018). Random Forests in the Classification of Diabetic Retinopathy Retinal Images. In Advanced Computational and Communication Paradigms (Vol. 475, pp. 168–176). Singapore: Springer Singapore.
67. Scornet, E. (2017). Tuning parameters in random forests. ESAIM: Proceedings and Surveys, 60, 144–162.
68. Buczak, A. L., & Guven, E. (2016). A Survey of Data Mining and Machine Learning Methods for Cyber Security Intrusion Detection. IEEE Communications Surveys & Tutorials, 18(2), 1153–1176.
69. Hassine, K., Erbad, A., & Hamila, R. (2019). Important Complexity Reduction of Random Forest in Multi-Classification Problem. In 2019 15th International Wireless

Communications & Mobile Computing Conference (IWCMC) (pp. 226–231). Presented at the 2019 15th International Wireless Communications and Mobile Computing Conference (IWCMC), Tangier, Morocco: IEEE.
70. Do, H. N., Vo, M.-T., Vuong, B. Q., Pham, H. T., Nguyen, A. H., & Luong, H. Q. (2016). Automatic license plate recognition using mobile device. In 2016 International Conference on Advanced Technologies for Communications (ATC) (pp. 268–271). Presented at the 2016 International Conference on Advanced Technologies for Communications (ATC), Hanoi, Vietnam: IEEE.
71. ZhiYu Chen, Abidi, B. R., Page, D. L., & Abidi, M. A. (2006). Gray-level grouping (GLG): an automatic method for optimized image contrast Enhancement-part I: the basic method. IEEE Transactions on Image Processing, 15(8), 2290–2302.
72. X. Chen, S. Li, & J. Hu. (2014). A survey on Otsu image segmentation methods. In Journal of Computational Information Systems.
73. Suzuki, S., & be, K. (1985). Topological structural analysis of digitized binary images by border following. Computer Vision, Graphics, and Image Processing, 30(1), 32–46.